

# Gemini: Integrating Full-fledged Sensing upon Millimeter Wave Communications

Yilong Li<sup>1</sup>, Zhe Chen<sup>2</sup>, Jun Luo<sup>3</sup>, Suman Banerjee<sup>1</sup>

University of Wisconsin-Madison<sup>1</sup>, USA, Fudan University<sup>2</sup>, China,  
Nanyang Technological University<sup>3</sup>, Singapore

## ABSTRACT

Integrating millimeter wave (mmWave) technology in both communication and sensing is promising as it enables the reuse of existing spectrum and infrastructure without draining resources. Most existing systems piggyback sensing onto conventional communication modes without fully exploiting the potential of integrated sensing and communication (ISAC) in mmWave radios (not *full-fledged*). In this paper, we design and implement a *full-fledged* mmWave ISAC system Gemini; it delivers raw channel states to serve a broad category of sensing applications. We first propose the mmWave self-interference cancellation approach to extract the weak reflected signals for near-field sensing purposes. Then, we develop a joint optimization scheduling framework that can be utilized in accurate radar sensing while maximizing the communication throughput. Finally, we design a united fusion sensing algorithm to offer a better sensing performance via combining monostatic and bistatic modes. We evaluate our system in extensive experiments to demonstrate Gemini's capability of simultaneously operating sensing and communication, enabling mmWave ISAC to perform better than the commercial off-the-shelf mmWave radar for 5G cellular networks.

## 1 INTRODUCTION

The past decade has witnessed significant progress in millimeter wave (mmWave) technology since it offers wider bandwidth and more antennas (e.g., 2GHz bandwidths and 16-element antennas [26]), compared with commodity sub-10GHz technologies (e.g., Wi-Fi 6 [5, 9]). On the one hand, these features enable mmWave communications to support a wide range of high-throughput applications, such as ultra HD video streaming, virtual and augmented reality [11, 48]. On the other hand, the same features also endow mmWave sensing with high spatial resolution, making mmWave radars necessary components of smart vehicles and robots [31, 32, 47]. While progress in communication and sensing used to be fairly independent, both academia and industry have started exploring the promising *integration of sensing and communication* (ISAC) for the next generation of mmWave systems [30, 36], enabling the use of existing spectrum and infrastructure, avoiding the cost of new hardware.

A number of existing theoretical proposals on mmWave ISAC systems for 6G and beyond have appeared [29] focus

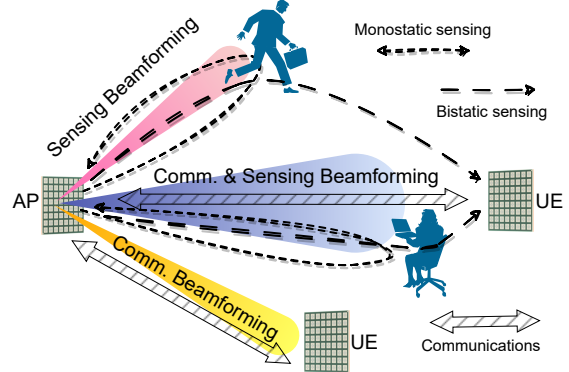


Figure 1: Vision of full-fledged mmWave ISAC system.

mainly on focus on waveform design, rather than guiding the practical systems to merge one function (e.g., sensing) with devices designed for another purpose (e.g., mmWave Wi-Fi [50, 52]). Among the few existing mmWave ISAC systems, most are designed to piggyback sensing onto communication infrastructure, hence confining sensing to only the *multi-static* communication setting with transmitter (Tx) and receiver (Rx) physically separated [36]. Only one SDR-based system by far has emulated a radar-like *monostatic sensing* capability [20], where the Tx and Rx are co-located to enable precise range estimation, yet it bears no intention in realizing ISAC: its waveform is designed only for sensing, rendering it largely incompatible with the existing commodity mmWave devices [1, 37]. In a nutshell, while theoretical studies on ISAC barely contribute to the development of real systems, existing system design stays at *adapting* phase far from a full *integration*.

Unlike conventional sub-10GHz Wi-Fi often getting only a couple of antennas, mmWave communication systems have their access point (AP) and user equipment (UE) both equipped with multiple phased arrays (a.k.a. hybrid beamforming for massive MIMO [22, 39]). As a result, typical mmWave ISAC scenarios shown in Figure 1 have their communication links highly directional, making them sub-optimal for the multi-static sensing setting where sensing subjects are often off the link. Therefore, a full-fledged mmWave ISAC system would need to better leverage the beamforming capability to handle sensing and communication in a truly integrated manner. In particular, the beam patterns should

be designed to support three functions: i) pure communication, ii) pure sensing under monostatic (reflection) sensing mode, and iii) simultaneous communication and sensing under monostatic and multi-static modes, as illustrated in Figure 1.

Implementing such a truly integrated mmWave ISAC system faces three major challenges. Firstly, unlike long-range sensing where direct Tx interference can be readily removed thanks to the fine-grained temporal resolution resulting from mmWave’s wide bandwidth, short-range sensing commonly adopted for indoor scenarios has to cope with the Tx interference potentially overwhelming the reflected sensing signals [16]. Second, though beam scheduling exists for mmWave communications, satisfying the three functions of mmWave ISAC demands a largely enhanced fair scheduling algorithm to weigh among all necessary beam patterns. Last but not least, both monostatic and multi-static modes may coexist and thus generate complementary sensing information concerning the same subject, incurring the need for a unified framework to fuse such diversified information in a constructive manner.

To this end, we build Gemini as a system that effectively integrates full-fledged sensing and communication at mmWave band. Gemini employs both a smart beamforming and a deep neural model to cancel the 2GHz wideband Tx interference; this allows the weak reflected signals from sensing subjects to be effectively extracted for short-range sensing. Extending the idea of smart beamforming, Gemini further innovates in a set cover inspired beam scheduling algorithm, in order to satisfy both sensing accuracy and communication throughput. Finally, Gemini is equipped with a distributed fusion mechanism for unified estimation, leveraging diversified information gathered from both monostatic and multi-static sensing modes. All these are wrapped into a mmWave ISAC protocol largely compatible with existing 802.11ay [10], implemented upon Sivers IMA EVK06003 [4] that operates at 60GHz band and is equipped with 16-element phased arrays. Our major contributions are summarized as follows:

- To the best of our knowledge, Gemini is the first mmWave ISAC system with a full-fledged sensing capability integrated with default communication function.
- We propose an interference cancellation scheme driven by deep neural model to combat the wideband and non-linear Tx interference to short-range sensing.
- We invent an application-aware beam scheduling algorithm for jointly optimizing sensing accuracy and communication throughput.
- We design a unified estimation framework to leverage the sensing diversity offered by both monostatic and multi-static modes.

- We evaluate our Gemini prototype with extensive experiments. The results confirm that Gemini gains full-fledged mmWave ISAC capability under realistic scenarios, such as point cloud and human tracking.

Noted that Gemini delivers raw channel states to enable various sensing application; it is not meant for any specific sensing purpose. The rest of our paper is organized as follows. Section 2 provides background and motivations for mmWave ISAC systems. Section 3 presents the critical components of Gemini. Section 4 specifies how the prototype is implemented. Section 5 reports the evaluation results on different applications. We briefly discuss general literature respectively on mmWave platforms and ISAC in Section 6, where we also explain limitations and future directions of Gemini. Finally, Section 7 concludes our paper.

## 2 BACKGROUND AND MOTIVATIONS

We start with the background on mmWave communication, and we then provide motivating examples to concretely demonstrate the challenges faced by the mmWave ISAC system design.

### 2.1 Basics of mmWave Communication

The following procedure summarizes default mmWave communication of IEEE 802.11ay [10].

- **Carrier Sense:** In order to avoid collisions, mmWave devices (including AP and UEs) configure quasi-omnidirectional patterns to their Rx phased arrays, and perform listen-before-talk principle.
- **Sector Sweep:** This phase determines the alignment direction of the main beams between AP and UE. If channel is idle, AP broadcasts *sector sweep* (SSW) frames with different narrow beams to scan all bearings, and UEs respond with signal strength indicators.
- **MIMO Setup & Training:** The AP selects UEs intended for transmissions, and sends special frames to notify them. This is followed by the AP transmitting training (TRN) sequences to these UEs for channel state information (CSI) estimation, and the UEs report results back to the AP.
- **Beamforming:** The optimal MIMO configurations are set by the AP, and beamforming is performed.

The implications of the above procedure are twofold: i) only one mmWave device is allowed to transmit due to carrier sensing and later responses from an UE, and ii) the bearings of all UEs<sup>1</sup> are obtained in the sector sweep phase. Therefore, it is reasonable to consider that all UE locations are known to the AP; this applies to all subjects too (see Section 3.1.2).

<sup>1</sup>In fact, the ranges between the AP and all UEs can be also obtained via the two-way time of arrival ranging method [17].

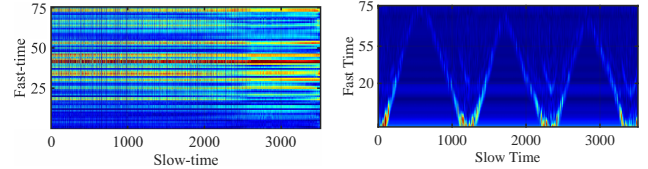
## 2.2 Tx Interference on Short-range Sensing

To realize the radar-like monostatic sensing function, Rx needs to be co-located with Tx to receive the reflected signals incurred by transmissions [2], but this arrangement naturally leads to *Tx interference* that potentially overpowers the reflected sensing signals. For long-range monostatic sensing envisioned for 5/6G base stations [20] where subjects are hundreds or even thousands of meters away from the signal source, one may leverage the fine-grained range bins [2] offered by the wide bandwidth of mmWave to handle Tx interference. Unfortunately, short-range monostatic sensing, often used indoors, is challenged by strong transmission interference, which can spread across several bins and overwhelm the sensing signals.

Though the same challenge also exists for enabling ISAC upon sub-10 GHz IoT devices [16], the Tx interference of mmWave is more complicated, due to the much higher carrier frequency and wider bandwidth. Such interference is quite different in nature too, as existing mmWave communication platforms (e.g., [26, 27]) often have separated Tx and Rx chains with their respective phased arrays, the Tx interference takes place in a *cross-chain* manner, instead of the intra-chain style for IoT devices [16]. To better understand how Tx interference affects the short-range monostatic sensing performance, we take the “push-pull” hand gesture as an example, and measure the signal magnitude variations caused by it, using Gemini whose implementation will be introduced in Section 4.

Our experiments follow 802.11ay standard [10]: OFDM is adopted for transmission and the CSI is obtained from the TRN field of a packet. For sensing purpose, we apply the inverse FFT to each CSI to obtain the CIR (channel impulse response) as the *fast-time* dimension, and combine multiple CIRs as the *slow-time* dimension. For the sake of clarity, we specifically differentiate between *Tx-beamforming* and *Rx-beamforming*, where only the respective phased arrays are leveraged to achieve the “focusing” effect in this experiment.

We first control the main beams of Tx-beamforming and Rx-beamforming at  $0^\circ$  orientation to point to the hand, and show the heatmap of CIR matrix in Figure 2(a). As expected, the heatmap exhibits random patterns that totally annihilate any features from the push-pull hand gesture, clearly demonstrating the damaging effect of the strong Tx interference to saturate the Rx chain. We then use Tx and Rx beamforming to cancel the Tx interference as much as possible. As shown in Figure 2(b), although certain beamforming patterns may help “single out” the features of the push-pull hand gesture, minor residual interference still persists to affect the CIR matrix used for sensing. More importantly, as beamforming is commonly used by mmWave communication systems to enhance channel quality, borrowing the same technique



(a) Without proper beamforming. (b) With proper beamforming.

**Figure 2: Sensing results, in the form of CIR matrices, of push-pull hand gesture, w/ and w/o beamforming.**

for sensing purpose may cause conflict between these two objectively; which leads to our next challenge.

## 2.3 Beam Scheduling Matters

Recalling that most of the current mmWave research proposals treat communication and sensing independently: they either focus on improving network throughput [33, 47, 53], or dedicate the mmWave devices to serve bistatic sensing [36]. Only one recent proposal [51] considers simultaneous communication and sensing, but the sensing is only piggybacked on communications by leveraging the side lobes to conduct low-effective sensing: it trades latency for temporal diversity so as to enhance sensing quality, at the cost of handling only static sensing subjects. For full-fledged ISAC mmWave systems, we need to balance the need from three functions, namely pure communication, pure sensing, and simultaneous communication and sensing. In the following, we conduct two experiments using the same setting, as in Section 2.2 to demonstrate the inherent conflict among these functions.

Given a setup consisting of an AP, a subject, and a UE arranged in an isosceles triangle configuration, the performance evaluation is carried out in two distinct cases: Case 1 chooses the best alignment between the main beams of the AP and UE for communications, while Case 2 has the AP and UE beamforming towards the subject for sensing hand gesture (only AP Tx and Rx beamforming is needed for monostatic sensing). The performance of these cases are depicted in Figure 3 for both monostatic and bistatic modes. It is evident that Case 1 gains much higher throughput than Case 2 in both sensing modes, but it is the reverse situation for hand gesture sensing. Also, Figure 3(d) serves as a counterexample for the effectiveness of the sidelobe sensing [51]. Apparently, the distinct beam patterns and the one-dimensional scheduling (only in bearings) are the key factor for the performance in both cases, indicating the need for a new beam scheduling algorithm to serve the best interest of both communication and sensing under both sensing modes.

## 2.4 Complementary Sensing Modes

Whereas the monostatic mode has many advantages (mostly in terms of the synchrony between Tx and Rx) [16], there exist certain situations where the bistatic mode may provide

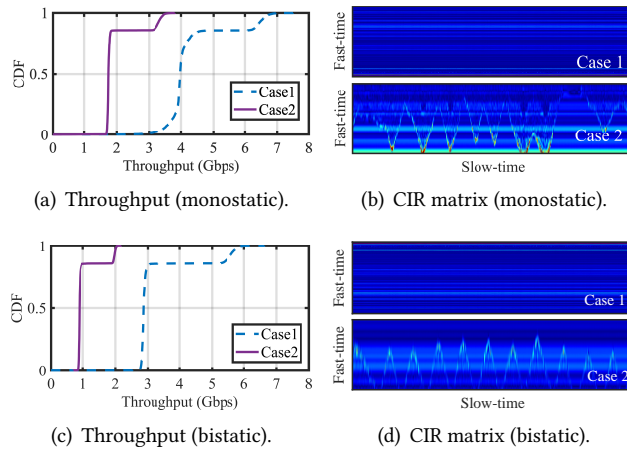


**Figure 3: The communication throughput and sensing CIR heatmaps in monostatic and bistatic modes.**

complementary sensing information: this is the *diversity gain* achievable due to the different “viewpoints”. Given the same experimental setting as Section 2.3, we measure the reflection power and the signal-to-noise ratio for sensing (S-SNR), computed similarly to that for communication) in a setup where the subject stands sideways with the shoulder facing the AP to minimize the impact of the hand gesture to the monostatic sensing signals (hence rendering it disadvantageous); the measurements for both monostatic and bistatic modes are shown in Figure 4. Clearly, the bistatic mode outperforms the monostatic mode in both reflection power and SNR, with 3 dBm gain in average power (nearly doubling that of monostatic mode’s 3.3 dBm power), as shown in Figure 4(a), and more than 2dB gain in average S-SNR upon that of the monostatic mode’s 2.05 dB, as shown in Figure 4(b).

These results can be explained by the relation between the motion direction of hand and the direction of signal reflections. As motion sensing with mmWave signals relies on the signal magnitude variations caused by motion, the better the motion direction is aligned with that of reflection, the stronger the reflection variations are. In reality, the chances for an arbitrary motion direction to be aligned with either monostatic or bistatic sensing mode is surely higher than with only one of them, because combining distinct reflection directions could improve the signal diversity. Since an ISAC

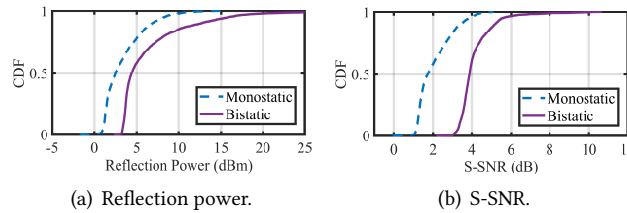


**Figure 4: The reflection power and S-SNR in monostatic and bistatic modes, respectively.**

system should definitely leverage this sensing diversity to offer effective sensing capabilities, it is imperative to have a unified framework for merging monostatic and multi-static sensing modes in a constructive way.

### 3 GEMINI: MMWAVE ISAC DESIGN

Motivated by the observations made in Section 2, our Gemini design comprises five key components: i) a sensing-aware channel probing scheme, ii) a two-stage Tx interference cancellation, iii) a holistic beamforming and scheduling mechanism for both sensing and communications, iv) an algorithm to exploit the diversity in sensing modes, and v) a hardware platform to support previous components. Given the overall construction of Gemini shown in Figure 5, the first four components are held in the three leftmost blocks, and they control the remaining (mostly hardware) blocks to perform beamforming and cancel interference, aiming to satisfy the diversified ISAC requirements. In the following, we introduce the first four components respectively but postpone the platform implementation details to Section 4.

#### 3.1 Channel Modeling and Probing

In this section, we design a probing scheme to obtain mmWave MIMO channel states for both sensing and communication, based on a properly defined channel model.

**3.1.1 Modeling mmWave MIMO Channels.** Compared with conventional (communication) channel, the mmWave MIMO channels for ISAC can be far more complicated, as they include at least four components: Tx interference, monostatic sensing (reflection), communication, and multi-static sensing (reflection). In a typical indoor mmWave MIMO setting, the AP has  $N$  Tx/Rx chains, each of them equipped with an  $M$ -elements phased array. For ISAC-oriented temporal scheduling, the AP selects  $N_U$  UEs and  $N_S$  subjects (where  $N = N_U + N_S$ ) from all UEs and subjects to serve at each time slot. Since the MU-MIMO via hybrid beamforming is adopted by IEEE 802.11ay [10], we consider the AP performing the MU-MIMO to the UEs. We let  $\mathbf{s}(t) = [s_1(t), \dots, s_N(t)]$ ,  $\mathbf{y}^u(t) = [y_1^u(t), \dots, y_{N_U}^u(t)]$ , and  $\mathbf{y}^s(t) = [y_1^s(t), \dots, y_{N_S}^s(t)]$  respectively represent the Tx signals from the AP, the Rx signals at the UEs, and the monostatic sensing signals received by the AP. Note that,  $\mathbf{y}^u(t)$  and  $\mathbf{y}^s(t)$ , even when happening to the same device, are temporally separated by the MAC protocol (see Section 2.1), while  $\mathbf{y}^u(t)$  is the superposition of the multi-static sensing signals  $\mathbf{y}^{us}(t)$  and the pure communication signals  $\mathbf{y}^{uc}(t)$ , i.e.,  $\mathbf{y}^u(t) = \mathbf{y}^{us}(t) + \mathbf{y}^{uc}(t)$ . In total, we can characterize the simultaneous ISAC (both AP and UE) Rx signals by:

$$\begin{aligned} \mathbf{y}(t) &= [\mathbf{y}^u(t), \mathbf{y}^s(t)]' \\ &= \mathbf{W}_{DB}^{Rx} \mathbf{W}_{AB}^{Rx} \mathbf{H}(t) \mathbf{W}_{AB}^{Tx} \mathbf{W}_{DB}^{Tx} \mathbf{s}(t) + \mathbf{W}_{DB}^{Rx} \mathbf{W}_{AB}^{Rx} \mathbf{n}(t), \end{aligned} \quad (1)$$

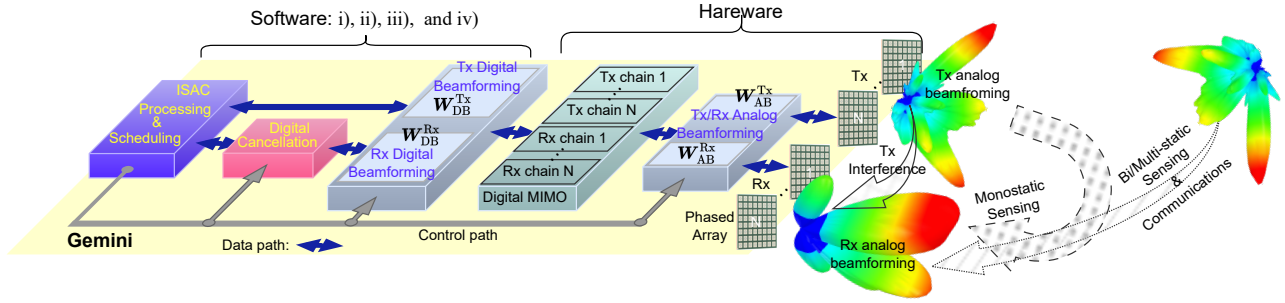


**Figure 5: Architecture of Gemini with four software components and one hardware platform.**

where  $\mathbf{W}_{DB}^{Rx}$ ,  $\mathbf{W}_{DB}^{Tx}$ ,  $\mathbf{W}_{AB}^{Rx}$ , and  $\mathbf{W}_{AB}^{Tx}$  are the Rx digital beamformers, the Tx digital beamformers, the Rx analog beamformers, and the Tx analog beamformers, respectively,  $[\cdot]'$  denotes matrix transpose, and  $\mathbf{n}(t)$  is the additive Gaussian noise with variance  $\sigma^2$ . It is worth noting that  $\mathbf{W}_*^{Rx}$  is of block-diagonal form, as it involves the beamformer of one device (e.g., UE) for  $\mathbf{y}^u(t)$  and that of another (e.g., AP) for  $\mathbf{y}^s(t)$ .

The  $H(t)$  in Eqn. (1) represents the mmWave MIMO channel; it involves the following major components:

$$H(t) = H_{ti}(t) + H_s(t) + H_c(t) + H_{ms}(t), \quad (2)$$

where the 4 terms on the right-hand side denote the Tx interference channels, monostatic sensing channels, communication channels, and multi-static sensing channels, respectively. According to Section 2.2,  $H_{ti}(t)$  may strongly affect  $H_s(t)$ , but the impact from  $H_c(t)$  to  $H_{ms}(t)$  can be readily handled [50]. Moreover, Eqn. (1) confirms what we have observed in Section 2.3: the hybrid beamformers can be scheduled to largely reshape the channels so as to affect performance in both communication and sensing. Consequently, though the two groups of channels, i.e.,  $\{H_{ti}(t), H_s(t)\}$  vs  $\{H_c(t), H_{ms}(t)\}$ , are seemingly independent of each other as they are physically or temporally separated, they become correlated as they may share the same Tx beamformers  $\mathbf{W}_*^{Tx}$ . In a nutshell, the goal of Gemini is to *optimize the hybrid Tx/Rx beamformers on all these channels in  $H(t)$  for balancing the performance between sensing and communication*. We take a divide-and-conquer method to approach this optimization, by eliminating  $H_{ti}(t)$  in Section 3.2 and jointly scheduling  $\{H_s(t), H_c(t), H_{ms}(t)\}$  in Section 3.3. However, before executing this plan, a scheme to probe the channel states needs to be in place.

**3.1.2 Probing mmWave ISAC Channels.** Recall that a probing scheme is employed for mmWave communications to acquire  $H_c$  in Section 2.1 under the sector sweep phase, which also yields  $H_{ms}(t)$  and the bearings of subjects via static background removal [12] and signal detection [38]. Since  $\{H_{ti}(t), H_s(t)\}$  cannot be directly acquired by this scheme, we piggyback an additional probing scheme on the existing one by emulating its behavior. Consequently, we mainly focus on this added scheme aiming to estimate the Tx interference

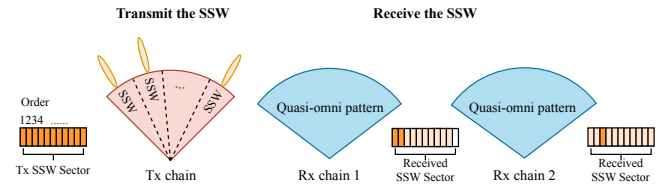


**Figure 6: Tx interference probing via extended SSW: “SSW sector” bars show the interference strength for each direction.**

channels  $H_{ti}(t)$  for the follow-up cancellation that obtains monostatic sensing channel  $H_s(t)$  in Section 3.2. A byproduct of this two-round probing and the later resulting  $H_s(t)$  is the locations of all subjects, as subject ranges can be inferred from  $H_s(t)$ 's time-of-flight.

Since the phased array equipped at Tx chain has multiple beam patterns and each of them causes different Tx interference, a probing scheme needs to collect all kinds of corresponding Tx interference channels. Therefore, our added scheme involves an additional round of SSW with a substantially lower Tx power to create a “wireless shortcut” for probing  $H_{ti}(t)$ , in order to avoid the interference from surrounding environments. As shown in Figure 6, upon transmitting SSW frames with Tx sector ID sequentially from a device (the pink sectors), the phased arrays of its Rx chains are set to quasi-omni-directional patterns to receive SSW frames (the blue sectors). In this way, the channel estimation field with TRN of SSW is utilized to extract the Tx interference channels  $H_{ti}(t)$  via a minimum mean square-error estimation [44].

Whereas the UE channel in Figure 7(a) is discovered by the 1st round SSW, the two sensing channels in Figure 7(b) are probed during the same SSW round. Apparently, the beamforming for UE may allow for sensing ‘Subject1’ at the same time, yet sensing ‘Subject2’ has to be scheduled in a different time slot. Moreover, the 2nd round SSW obtains Tx interference states shown in Figure 7(c): the impact appears to be more intensive at  $0^\circ$  and is otherwise quasi-symmetric on two sides. We also measure the correlation between any

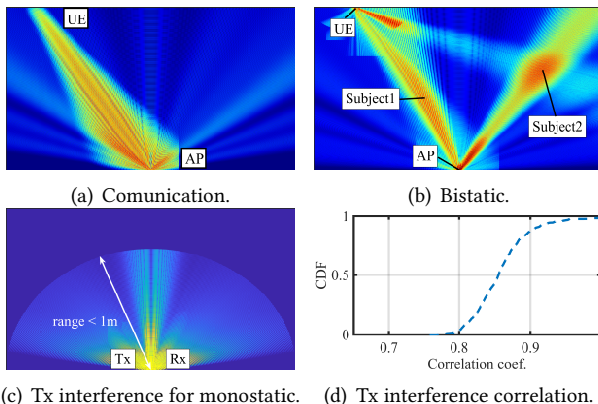


**Figure 7: Beamforming heatmaps of (a-b) default probing for communications and multi-static sensing, (c) new probing scheme for Tx interference, with (d) statistics on interference stability.**

two Tx interference channels at different time slots, and the results in Figure 7(d) demonstrate correlation coefficients mostly above 0.8. Therefore, the information provided by one round SSW can help train a cancellation process that remains valid for a long period.

### 3.2 Monostatic Sensing for mmWave ISAC

In this section, we introduce a two-stage Tx interference cancellation process to enable monostatic sensing: namely beam nulling and deep denoising.

**3.2.1 Beam Nulling.** We leverage the hybrid beamforming to reduce the Tx interference at the first stage. Since advanced phased array allows for controlling both amplitude and phase [49] via antenna weights vectors (AWV), we leverage this ability to offer efficient solutions for future developments. To achieve beam nulling for the  $i$ -th sector containing at least a subject, we leverage the hybrid beamforming to minimize Tx interference  $H_{ti}^i(t)$ :

$$\min_{W_{DB}^{Rx}, W_{AB}^{Rx}, W_{AB}^{Tx}, W_{DB}^{Tx}} \|W_{DB}^{Rx} W_{AB}^{Rx} H_{ti}^i(t) W_{AB}^{Tx} W_{DB}^{Tx}\|_F^2, \quad (3)$$

where  $\|\cdot\|_F$  is the Frobenius norm. Since the hybrid beamformers involve a large amount of parameters to be optimized, searching for an optimal solution directly using conventional optimization methods can be highly inefficient. Moreover, since these parameters will also be needed for the joint scheduling in Section 3.3, the degree of freedom in fine-tuning them is limited.

Fortunately, we find the problem (3) can be approached as training a neural network, given the similarity between the data pipeline (see Figure 5) and a linear autoencoder [25]. We reformulate Eqn. (3) into an inverse neural network shown in Figure 8, where the Tx interference channels and the Tx/Rx hybrid beamformers are respectively modeled as the

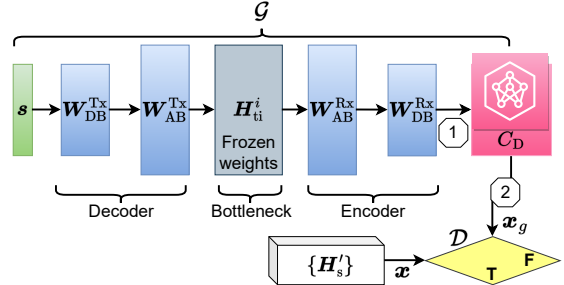


**Figure 8: The two-stage Tx interference cancellation via linear autodecoder (LAE) and cGAN.**

bottleneck layer (weights frozen as the channel  $H_{ti}^i(t)$  is physically determined) and decoder/encoder whose weights are beamformer parameters, while the Tx signals  $s$  become the TRN. The objective of a hypothetical training process should result in the output  $x$  being the  $H_s(t)$  after canceling the overwhelming  $H_{ti}^i(t)$ . However, the network cannot be trained without any ground truth dataset for  $H_s(t)$ .

**3.2.2 Deep Denoising.** By far, we have reformed the problem to reconstructing  $H_s(t)$  from the observation  $H'(t) = H_{ti}^i(t) + g(H_s(t))$  where the  $g(\cdot)$  is a deterministic mapping introduced by the beamforming operations. Since obtaining the ground truth for  $H_s(t)$  is infeasible, we try to bypass this issue by using a mmWave radar at the 60 GHz with 2 GHz bandwidth [2] to collect a dataset for  $H'_s(t)$ : since the radar is designed for sensing but with system parameters similar to Gemini,  $H_s(t)$  and  $H'_s(t)$  should share high-level yet intrinsic features. It should be stressed that the mmWave radar is only deployed during the training stage and is surely not required by Gemini in runtime. Though we cannot directly use  $H'_s(t)$  as ground truth for supervised learning, exploiting it to perform adversarial learning is certainly feasible. To this end, we append an *digital cancellation* neural network  $C_D(t)$  to the above model (see Figure 8), and we train the whole model as a cGAN (conditional Generative Adversarial Network) [34]. Our model is trained to learn how to cancel Tx interference regardless of all environment inferences, so only one training is needed for each type of mmWave device. We denote by  $\mathcal{G}$  the whole neural network constructed so far; it generates samples  $x_g = \mathcal{G}(z|s)$  with  $z$  being the background Gaussian noise introduced by the signal processing/propagation pipeline (LAE). We further employ a discriminator network  $\mathcal{D}(x)$  aiming to recognize if  $x$  comes from  $\{H'_s(t)\}$ . According to [34],  $\mathcal{D}$  and  $\mathcal{G}$  play a min-max game modeled by:

$$\min_{\mathcal{G}} \max_{\mathcal{D}} \mathbb{E}_{x \sim p_{H'_s}} [\log \mathcal{D}(x|s)] + \mathbb{E}_{z \sim \mathcal{N}} [\log(1 - \mathcal{D}(\mathcal{G}(z|s)))],$$

where  $\mathcal{N}$  denotes the Gaussian noise distribution. Essentially, we use the cGAN as a powerful non-linear filter to obtain the monostatic sensing channels by “generating” it out of the channel states contaminated by  $H_{ti}^i(t)$ .

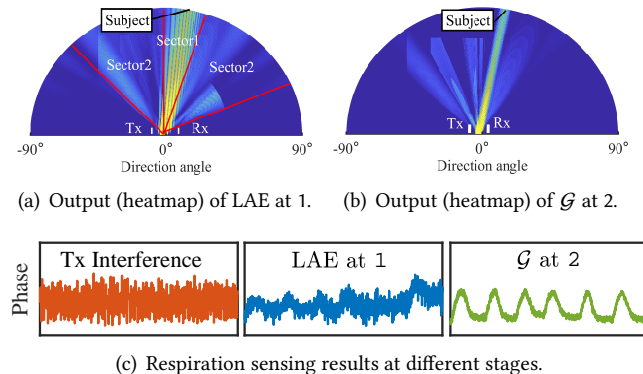


**Figure 9: Beamforming heatmaps of our two-stage Tx interference cancellation (a-b) and the resulting respiration sensing outcome (c).**

To verify the effectiveness of our design, we let a subject stand in the front of our platform with  $15^\circ$  bearing and extract its respiration via the proposed pipeline. We first show the heatmaps of our two-stage cancellation in Figures 9(a) and 9(b); it clearly demonstrates the gradually “diminishing” of  $H_{ti}^l(t)$  through the pipeline. Further plotting the respiration sensing results in Figure 9(c) confirms the largely suppressed Tx interference<sup>2</sup>.

### 3.3 Beam Scheduling for mmWave ISAC

Since 802.11ay has a default beam scheduling scheme for MU-MIMO, our new scheduling scheme simply piggybacks on the existing one, aiming to integrate sensing and communication beamforming in the most efficient manner, as briefly envisioned by Figure 10. In the following, we first study how sensing subject selection differs from UE selection, then a scheduling algorithm is designed for efficient coverage of both sensing and communications.

**3.3.1 Subject and UE Selection.** UE selection has a default implementation in 802.11ay as MU-MIMO. In particular, MU-MIMO starts with AP using the SSW (see Section 2.1) to obtain channel states from UEs and grouping UEs with correlated channels (of similar bearing) [42] as a set to be covered by the same analog beam pattern. Then the bearing scheduling arranges UEs from the orthogonal (non-correlated) sets to communicate via distinct Tx chains simultaneously. For UEs covered by the same beam pattern or unable to be scheduled spatially, a temporal scheduling operating in a round-robin fashion is adopted to serve them. In summary, the communication-oriented UE selection operates in a *single dimension* manner for bearing scheduling, leading to inefficiency in handling the conflict among pure communication,

<sup>2</sup>While Gemini enables Tx interference cancellation, packet detection delays may introduce ranging errors. This is mitigated through an RF loopback calibration technique [20] in the RF front-end to correct the corresponding phase offsets; it processes Rx signals before ranging.

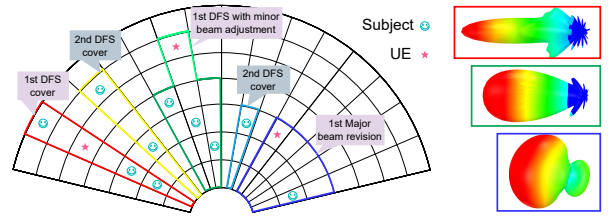


**Figure 10: BC-Sets for ISAC-oriented beam scheduling.**

pure sensing, and simultaneous communication and sensing (see Section 2.3) under ISAC context.

Unlike communication, sensing allows subjects with the same bearing but different ranges to be differentiated, given a sufficient range resolution. With the 2GHz bandwidth of Gemini, the resulting centimeter-level resolution may enable many subjects to be simultaneously covered by one beam pattern, adding one more dimension for the ISAC scheduling. In addition, locations of UEs and subjects are known (see Sections 2.1 and 3.1.2). Consequently, we upgrade the correlated set definition to a *two-dimensional* Beam-Compatible Set (BC-Set) in the beamforming phase; it aims to group both UEs and subjects under a single beam pattern that may serve one UE and all the covered subjects simultaneously. We plot five BC-Sets in Figure 10; they are meant for illustrative purpose only, as realistic beam patterns (shown on the right part) can be far more irregular.

**3.3.2 Communication and Sensing Scheduling.** To determine the BC-Sets and their corresponding beam patterns, we start from the default communication scheduling that outputs the correlated communication sets  $\mathcal{U} = \{U_1, \dots\}$  [10]. As illustrated in Algorithm 1, our algorithm essentially executes in a greedy manner: it first adds as many subjects as possible to sets in  $\mathcal{U}$  for forming the initial BC-Sets, then it constructs new BS-Sets to cover the remaining subjects. It first gathers all positions covered by beam patterns of individual sets in  $\mathcal{U}$  (line 2). Then it performs a range-wise *depth-first search* (DFS) to gather subjects that can be covered by these sets (line 3), since initially beam patterns are often very narrow. If possible, it adjusts the original narrow beam pattern to trade its range for beam width, making it possible to conduct a bearing-wise breadth search for covering more subjects (line 9). Upon upgrading all sets in  $\mathcal{U}$  to BC-Sets, the algorithm again proceeds in the greedy DFS manner in the next stage, aiming to construct new BC-Sets to cover the remaining subjects (line 6 till the end).

What Algorithm 1 outputs are only (logical) BC-Sets; they need to be “translated” into (physical) beam patterns. Essentially, the beam patterns should be shaped by both the distribution of UEs/subjects covered by the BC-Sets and the capability of the phased array [19]. The procedure of shaping a beam pattern follows two basic principles: i) adopting

wider beams to trade range for width coverage and ii) adjusting the direction of the main beam to balance the coverage among multiple entities. Since the resulting patterns have not taken into account the beam nulling requirements (see Section 3.2), the corresponding beamformers are used as the initial setting for the problem (3) (hence the LAE) to derive proper cancellation schemes for individual BC-Sets. Finally, we analyze the complexity of Algorithm 1 to demonstrate its efficiency for real-time execution. Let the number of UEs be  $K$  and that for range (resp. bearing) bins be  $K_R$  (resp.  $K_D$ ), the complexity is  $O(KK_DK_R)$ , often up to the scale of several hundreds only.

We may walk through the algorithm using the BC-Sets in Figure 10 as examples. During the 1st stage, the three UE sets (red, green, and blue) are sequentially upgraded to form BC-Sets by adding in more subjects. Then the remaining three subjects are covered by two new BC-Sets (yellow and cyan). While the red and yellow BC-Sets can be covered by the default (narrow) beam sectors, others should be reshaped: in particular, both principles apply to the blue one. We also perform a trace-driven emulation to evaluate the advantages of BC-Sets. We set 6 UEs and 14 subjects in our experiment, and randomize their positions in each experiment. We run

---

**Algorithm 1:** BC-Sets construction.

---

**Input :**  $\mathcal{X}$ : Range-bearing matrix of all entities  
 $\mathcal{U}$ : Original communication sets for UEs  
 $r$ : Adjustable beam width

**Output:**  $\mathcal{B}$ : BC-Sets.

```

1 for  $U_i \in \mathcal{U}$  do
2    $C \leftarrow \text{beam\_pattern\_coverage}(U_i)$ 
3    $B_i \leftarrow \text{max\_depth\_range\_search}(C, \mathcal{X})$ 
4    $B_i \cup = \text{breadth\_bearing\_search}(C, \mathcal{X}, r)$ 
5    $\mathcal{B} = \{B_1, \dots, B_i, \dots\}$ 
6    $\bar{\mathcal{X}} \leftarrow \text{find\_non\_selected\_subjects}(B, \mathcal{X})$ 
7 while  $\bar{\mathcal{X}} \neq \emptyset$  do
8    $[C, B] \leftarrow \text{max\_depth\_range\_search}(\bar{\mathcal{X}})$ 
9    $B \cup = \text{breadth\_bearing\_search}(C, \mathcal{X}, r)$ 
10   $\bar{\mathcal{X}} \leftarrow \text{find\_non\_selected\_subjects}(B, \bar{\mathcal{X}})$ 
11   $\mathcal{B} \cup = \{B\}$ 

```

---

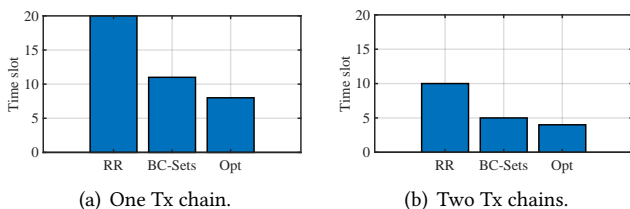


Figure 11: Average time spans of round-robin (RR), BC-Sets (scheduling) and the optimal solution (Opt).

three algorithms each for 100 trials, and show the average time spans for serving all UEs and subjects in Figure 11. Apparently, our scheduling requires only half of RR's time span and goes close to the optimal solution.

### 3.4 Exploiting Sensing Diversity

The scheduling algorithm presented in Section 3.3 has actually implicated two steps. On one hand, this scheduling takes place not only on the AP side but also on the UE side, albeit with less powerful beam fine-tuning ability. On the other hand, whereas covering monostatic sensing subjects can be determined in a unilateral manner, conducting bistatic sensing demands collaborative beamforming on both sides, similar to the default (bistatic) communication scheduling. As the locations of all subjects are estimated in advance (see Section 3.1.2), all these can be achieved naturally by Algorithm 1. Therefore, the question now is how to exploit the sensing diversity introduced by different sensing modalities, and our answer is the following unified estimation framework at signal processing level.

One of the major reasons that motivates us to consider full-fledged ISAC is the deficit of multi-static sensing in lack of synchronizations among different parties [16]. As a result, multi-static sensing can only be used to sense motion-induced information that incurs channel variations, whereas sensing (quasi-)static subjects can be fully achieved by monostatic sensing: for example, locating a subject can be done by AP estimating range/bearing and refined by the same estimations from UEs. Nevertheless, in motion tracking scenarios for both micro-motion [15] and macro-motion [23], joint estimation with diversified sensing results can only lead to improved accuracy [35]. Instead of dwelling on the design of estimation algorithms, we simply leverage existing estimation frameworks for this purpose. On the one hand, micro-motion estimation is taken care by SAGE [35], which requires a subject to remain quasi-static. On the other hand, macro-motion estimation (a.k.a motion tracking) is handled by the well-known extended Kalman filter [41]. We demonstrate how sensing diversity helps to improve precision of subject location estimation (via SAGE) in Figure 12: from left to right, the “hot spot” shrinks as the number of sensing modalities (hence the amount of beam intersections) increases, indicating a higher estimation precision.

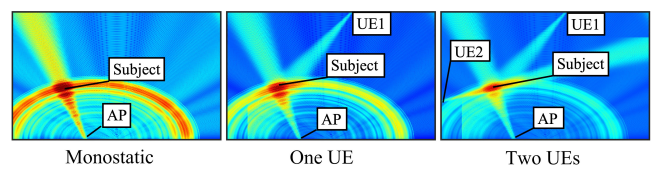
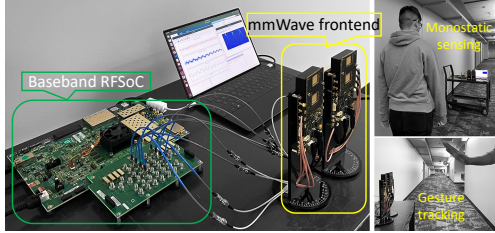


Figure 12: Improving estimation precision via joint monostatic and multi-static sensing.



**Figure 13: Part of the implementation and evaluation setup with mmWave frontend and baseband RFSoC.**

## 4 IMPLEMENTATION

We hereby elaborate on the implementation of Gemini, particularly explaining how to configure Gemini for carrying out the design objectives outlined in Section 3. The implementation follows IEEE 802.11ay standard operating at the unlicensed 60GHz frequency band, as demonstrated in Figure 13. We omit the illustration for the UE part, as it involves similar components but with only one mmWave frontend.

*Hardware Platform.* Gemini has three hardware components: mmWave front-end module, baseband processing module, and high-performance processor module. For the RF front-end, Gemini adopts the EVK06003 development kits from Sivers Wireless [4]; each kit has two 16-element phased arrays<sup>3</sup> The baseband processing and high-performance processor modules are both realized upon the Xilinx RFSoC ZCU208 development board [8]; it offers a multitude of advanced features and capabilities, including i) AD/DA converters for baseband sampling with a rate up to 4GHz, ii) DDR memory providing ample storage space for processed data, and iii) multi-core ARM processors and high-end Ultrascale FPGA offering substantial computational power.

*Software Components.* The software of Gemini is responsible for a variety of tasks, including beamforming, interference cancellation (Section 3.2), beamform scheduling (Section 3.3), data streaming to and from a PC controller. We implement above tasks using Verilog and C/C++, and compile them as a firmware for Xilinx ZYNQ RFSoC. We also implement a Matlab interface to pull the data from the RFSoC into the PC. The sensing algorithms, except for the deep neural module, are implemented in Matlab.

*Deep Neural Network.* Our deep neural network is built upon PyTorch [3] platform using Python 3.7, and an mmWave radar [2] is adopted to act as both a baseline and ground truth sensor. We synchronize the clocks of the radar and Gemini (both driven by a PC) via precision time protocol [21], hence aligning their starting time to  $\mu$ s level. The encoder/decoder of the LAE are actually formed by beamformers, so we only need to construct  $C_D(t)$  as a 5-layer perceptron and the discriminator with three CNN layers whose input size ( $2000 \times 1$

<sup>3</sup>Since many commercial transceiver chips of mmWave offer separated Tx and Rx phased arrays [4, 37], Gemini is equipped with two such arrays.

matches the output data of the radar. The batch size is set to 64 for training, and the model is optimized using the Adam optimizer with a learning rate of 0.001. We further quantize the neural network weights [46] to control the 4-bit phase and amplitude via AWV look-up table of mmWave frontend.

## 5 EXPERIMENT EVALUATIONS

We now perform three sets of experiments to verify the major functions of Gemini, namely Tx interference cancellation for monostatic sensing, beam scheduling for joint sensing and communications, and sensing diversity exploitation. Part of the experiment setup is depicted in Figure 13, but other necessary details shall be provided later. Our experiments have strictly followed the IRB of our institutes.

### 5.1 Monostatic Sensing

We report the outcome of Tx interference cancellation and the consequent monostatic sensing performance of Gemini. The experiments involve range, bearing, and speed estimations of a static or moving object (a metal block held by a person). The ground truths for range and bearing are measured by Intel RealSense LiDAR [7], while that for speed is provided by the TI radar [2]. We adopt absolute error as the evaluation metric.

**5.1.1 Tx Interference Cancellation.** We begin by quantifying the interference cancellation ability at different stages. We set the Tx power to 40dBm and observe the signal strength at different stages indicated in Figure 8. The results shown in Figure 14 confirm that LAE reduces Tx interference by about 39 dB, and deep denoising further suppresses it by 27 dB. Overall, the total cancellation is approximately 66 dB, and the remaining Tx-interference power goes very close to the noise floor. Apparently, the monostatic reflection channels  $H_s(t)$  has been distilled from  $H(t)$  in Eqn. (2).

**5.1.2 Range.** The ability to ranging is a fundamental and crucial sensing feature, but it can only be accomplished in the monostatic mode [16]. We study the ranging performance with/without Tx interference cancellation, given the subject staying statically in the range of [1, 5] m with a step size of 0.5m from Gemini, and Gemini performing ranging via CIR. We use the TI radar as a baseline by co-locating it with Gemini. The range errors shown in Figure 15(a) confirm that Gemini can obtain comparable performance to the radar, but

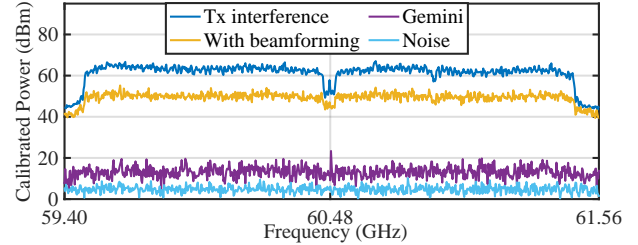


**Figure 14: Power spectrum of the received baseband signal after two-stage Tx interference cancellation.**

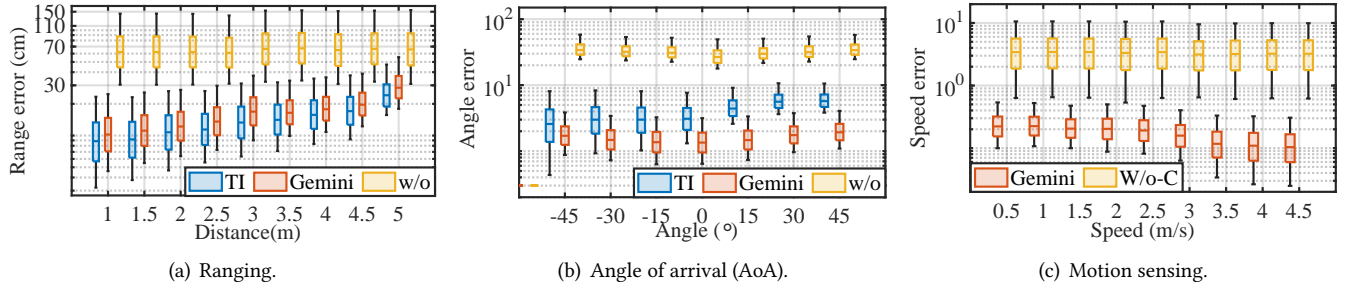


**Figure 15: Monostatic sensing performance.** “TI” and “W/o-C” denote the TI mmWave cascaded radar and Gemini without Tx interference cancellation, respectively. TI disappears from (c) as it is used as the ground truth collector.

much higher median range errors up to 30cm are introduced without the Tx interference cancellation. The range errors of both TI radar and Gemini slightly grow as the distance increases, potentially because the adopted beam pattern covers more background clutters at further distances and multipath reflections from them affect the ranging accuracy. Moreover, reflected (sensing) signals attenuate in distance and hence also result in degraded performance.

**5.1.3 Bearing.** To study another fundamental sensing function, we leverage the phased arrays equipped with both Gemini and the TI cascaded radar [2] to estimate object bearing (or AoA). We let the object stay within a bearing of  $[-45^\circ, 45^\circ]$  and vary with a step size of  $15^\circ$ . As shown in Figure 15(b), Gemini achieves better performance than that of radar because Gemini has a much more powerful phased array than that of radar. Again, Tx interference significantly degrades the bearing estimation performance if not properly handled.

**5.1.4 Speed.** The motion sensing is also crucial to the capability of Gemini, so we conducted tests where the object moves at a varying speed ranging from 0.5 m/s to 3.0 m/s within a  $3 \times 20\text{m}^2$  corridor. Since the LiDAR cannot monitor motion, we have to change the role of the TI radar from baseline to measuring the ground truth. The evaluation results shown in Figure 15(c) clearly demonstrate that Gemini achieves a much lower speed estimation error with the enhancement offered by the Tx interference cancellation.

*Remark:* During all above experiments, we have a communication session going on between the AP and UE. Since monostatic sensing takes place only on the AP side and it simply piggybacks on the Tx signals, the communication throughput is not affected at all.

## 5.2 Beam Scheduling for ISAC

One may expect a full-scale evaluation of our beam scheduling algorithm with many subjects and UEs involved simultaneously. Our experimental setup, depicted in Figure 16, is straightforward, involving one subject and one UE. Specifically, we demonstrate the simultaneous tracking of two subjects with two UEs in human tracking experiments to illustrate the potential for involving additional UEs. On one

hand, our scheduling algorithm excels in dispatching BC-Sets to cover subjects with compatible demands and hence all BC-Sets (or all subjects covered by a BC-Set) are similarly served by the AP. Consequently, evaluating the performance with one subject is sufficiently representative. On the other hand, serving multiple UEs bears no difference from serving one UE, as multiple UEs would inevitably need to be served by distinct Tx chains or in different time slots (see the media access described in Section 2.1). Also, due to the extremely high cost of our high-performance hardware (mmWave frontend [4] each costs over \$3300 and RF-SoC [8] costs \$15000), we cannot afford to support a lot of UEs. Therefore, we believe our evaluation scenario does produce results with practical significance. In the following, we evaluate our scheduling algorithm in three sensing applications, namely respiration monitoring, point cloud of human pose, and human tracking, along with a communication session. We consider three scheduling baselines: sensing only (SO), communication only (CO) [51], and round-robin (RR), while also adopting the TI radar as a sensing baseline.

**5.2.1 Respiration Monitoring.** This experiment takes the subject’s respiration as the sensing target, aiming to accurately estimate the breath rate. The results plotted in Figure 17 showcase the obtained throughput against corresponding sensing accuracy. We may observe that, while Gemini achieves a sensing accuracy almost the same as that for both SO and TI radar (which is much better than that for CO and RR), its throughput is only marginally lower than that of CO (but still much higher than that for SO or RR). In fact,

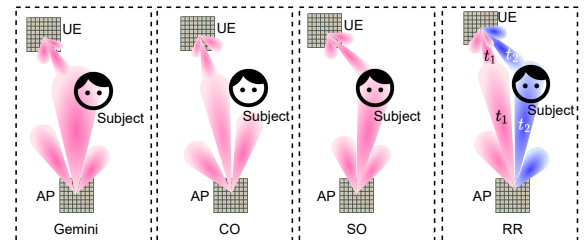


**Figure 16: An illustration of the experiment setup.**

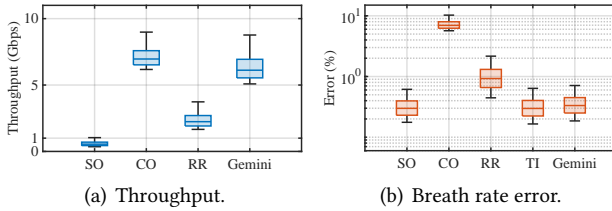


**Figure 17: Scheduling for simultaneous communications and respiration monitoring.**

for continuous yet spatially coarse-grained sensing applications, Gemini can always obtain nearly perfect sensing performance and barely sacrifice throughput.

**5.2.2 Point Cloud.** Different from continuous sensing application in Section 5.2.1, point cloud is a one-shot sensing application (e.g., 1 s duration in our experiment). In such applications, a much narrower beam is required to generate dense point cloud, yet Gemini still needs to maintain its beam schedules. Our solution is to have asymmetric Tx and Rx beam patterns for the AP: while the Tx one is designed to match that determined by the corresponding BC-Set, the Rx chain tunes its beam to the finest  $1.5^\circ$  beamwidth and quickly switches to distinct azimuth and elevation angles for “scanning” the subject under the BC-Set coverage. According to the reflection power at different angle pairs, we set a threshold to filter out reflection signals with very lower

power, and map the residue signals from polar coordinates to Cartesian coordinates so as to generate point cloud [18].

We test Gemini and the baselines in sequence and report the results in Figure 18: while throughput is statistics from all trials, the one-shot point cloud results are arbitrarily chosen examples (a human figure) for demonstration purpose only. Results in Figure 18(a) suggest that the throughput gap between Gemini and CO gets slightly wider, but Gemini still outperforms other two baselines: to generate 3D point cloud, Gemini has to temporarily sacrifice a bit throughput to capture fine-grained reflection signals. Though SO in Figure 18(c) performs marginally better than Gemini in Figure 18(b), the main beam of SO has to solely target the subject, hence resulting in the lowest throughput. RR sits in the middle of CO and SO for both throughput and point cloud performance shown in Figure 18(a) and Figure 18(e), due to its time-division nature. Finally, the TI cascaded radar with a number of antennas ( $12 \text{ Tx} \times 16 \text{ Rx}$ ) also performs poorly with its lower bearing resolution than Sivers’ phased array antennas [49] illustrated in Figure 18(f).

**5.2.3 Human Movement.** We captured the human movements in a room approximately  $21 \times 18$  feet, slightly larger than a typical US family room, accommodating scenarios with larger movements involving multiple UEs and several subjects. Human subjects follow the predefined paths marked on the floor, specifically ‘Rectangular’ and ‘Straight Line’ trajectories as depicted in Figure 19. Throughput and tracking

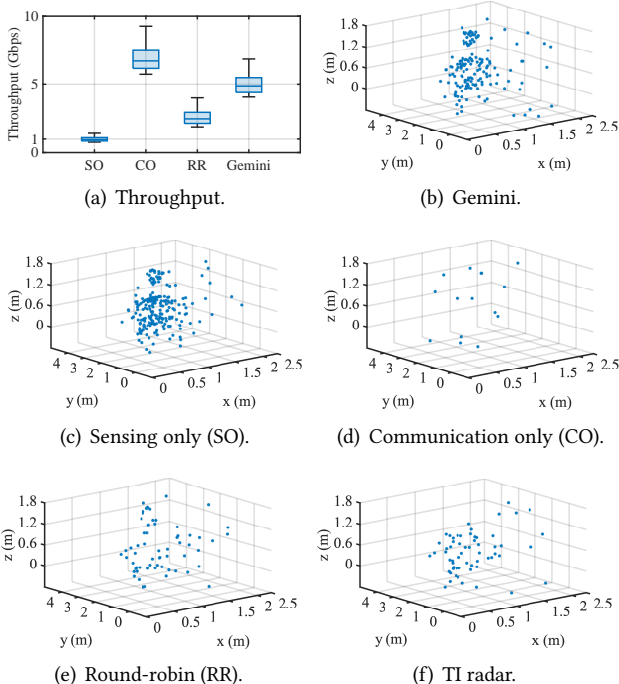


**Figure 18: Scheduling for simultaneous communications and point cloud generation (of a human figure).**

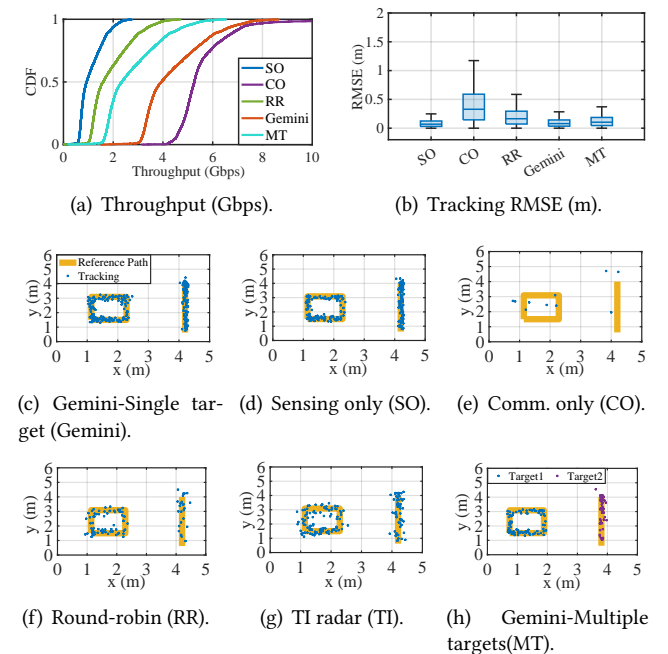


**Figure 19: Scheduling for simultaneous communications and human movement tracking in the test area. Orange lines show the ground truth—predefined paths—while blue points display tracking results.**

performance are depicted in Figure 19. As for the sensing performance shown in Figures 19(c) to 19(g), human movement exhibits a similar performance ranking as static point cloud generation, as it is also about producing point cloud but in both temporal and spatial dimensions. For the case involving multiple human subjects and UEs as shown in Figure 19(h), we placed two frontends as UEs to receive the data from the AP, with each subject following one of the two predefined paths. Despite the slight decreases in throughput and tracking accuracy observed with two UEs tracking two targets (MT), Gemini still outperforms baselines with only one UE and one target. It is attributed to our beam scheduling algorithm, which effectively balances communication and sensing tasks.

In fact, the idea of ISAC is not meant to benefit any specific applications; it is basically striking a balance between sensing and communication, *at the benefit of having them co-existing in one hardware*. Meanwhile, Gemini, with its innovative scheduling driven by BC-Set, is superior to existing mmWave-ISAC solutions, as it is demonstrated by our intensive experiments to have obtained performance very close to either SO (for sensing) or CO (for communications), given that both sensing and communication functions co-exist in one hardware and operate simultaneously.

### 5.3 Sensing Diversity

We hereby revisit the point cloud application to evaluate our unified estimation framework explained Section 3.4 for fusing multiple sensing modalities. Basically, we start from the AP monostatic sensing already shown in Figure 18(b) and gradually fuse in more UE (multi-static) sensing results. As expected, the density of the point cloud increases positively with the number of UEs from Figures 20(a) to 20(d), while the 3D point scattering getting quickly shrunk, rendering the overall human figure clearer step-by-step.

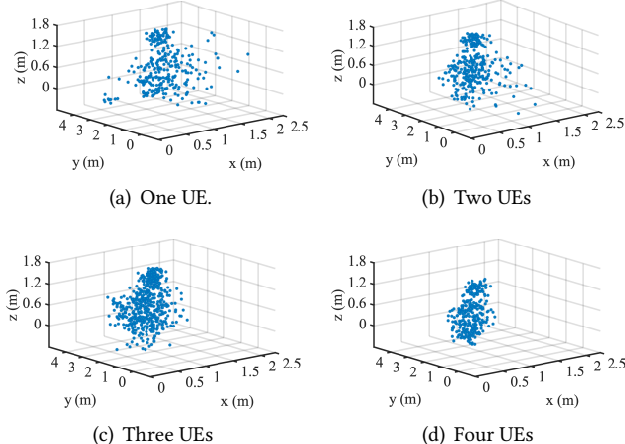


**Figure 20: Sensing diversity with different UEs may substantially enhance the point cloud quality.**

## 6 RELATED WORKS AND DISCUSSIONS

This section focuses on three main streams of related works, namely mmWave platforms, ISAC, and full duplex radio (FDR), with brief discussions on limitations of Gemini.

*mmWave Platforms.* Earlier mmWave platforms [40, 53] only offer a relatively wide bandwidth, yet their phased arrays cannot be precisely controlled for fast alignment, thus not exactly meeting the requirements of IEEE 802.11ad [6]. M-Cube [55] utilizes a commodity 802.11ad RF front-end with phased array antennas, but it was soon superseded by mmFlex [26] adopting similar mmWave front-end as Gemini to also match the more advanced standard of 802.11ay.

*ISAC.* Though theoretical works studying mmWave ISAC for 5/6G cellular network scenarios are plentiful [30, 54], they only focus on waveform design without providing useful guidelines for system developments. For ISAC on mmWave band, a couple of proposals [36, 51] have leveraged existing communication traffic to enable only multi-static sensing confined to subjects compatible with existing communication beam patterns. Though a monostatic sensing solution has been mentioned in [20?], it is far from fully integration into existing communication devices.

*Nulling and FDR.* Existing proposals on nulling for communications [33, 39, 43] are only marginally related and hence omitted from our discussions. Certain Wi-Fi sensing developments [13, 24] have gone very close to FDR [14], as they adopt either nulling or FDR to cancel Tx interference for motion sensing. However, as pointed out by [16], monostatic sensing for ISAC is fundamentally different from FDR.

*Gemini.* Gemini cannot leverage FDR-like technologies to extract monostatic sensing signals (explained in Section 3.2), so we exploit a hybrid (hardware-software) deep learning model to remove Tx interference. We also innovate in designing a beam scheduling for ISAC (see Section 3.3), and fusing multiple sensing modalities for improving estimation precision (see Section 3.4). In the meantime, we are considering fusing sub-6GHz Wi-Fi and mmWave to enhance the capability of ISAC, as it has been done for communication only [45]. Also, endowing Wi-Fi with sensing capability may cause unexpected information leakage [28], which can be exacerbated by the powerful mmWave-ISAC, so security issue should be part of our future work.

## 7 CONCLUSION

In this paper, we have proposed, designed and implemented Gemini, a full-fledge mmWave ISAC system. We have first given three concrete analyses to motivate our design. then we have elaborated all key components for Gemini, namely i) Tx interference cancellation driven by deep learning to enable monostatic sensing, ii) beam scheduling algorithm for jointly

optimizing sensing accuracy and communication throughput, and iii) a unified estimation framework for exploiting diversified sensing modalities. Finally, we have conducted extensive experiments to evaluate the performance of Gemini; our results have strongly demonstrated advantages of Gemini in actually taking care of both communication and sensing under its ISAC framework. We believe that our initial trials in realizing Gemini signify a pivotal step towards more practical mmWave ISAC systems.

## REFERENCES

- [1] Intel WiGig. <https://www.intel.com/content/www/us/en/products/docs/wireless-products/wigig-overview.html>.
- [2] IWR6843 Intelligent mmWave Sensor Standard Antenna Plug-in Module. <https://www.ti.com/tool/IWR6843ISK>.
- [3] PyTorch. <https://pytorch.org/>.
- [4] Sivers Semiconductors mmWave 60GHz Evaluation Kits (EVK). <https://www.sivers-semiconductors.com/sivers-wireless/evaluation-kits/>.
- [5] Wi-Fi CERTIFIED 6. <https://www.wi-fi.org/discover-wi-fi/wi-fi-certified-6>.
- [6] IEEE Standard for Information Technology—Telecommunications and Information Exchange between Systems—Local and Metropolitan Area Networks—Specific Requirements—Part 11: Wireless LAN Medium Access Control (MAC) and Physical Layer (PHY) Specifications Amendment 3: Enhancements for Very High Throughput in the 60 GHz Band. *IEEE Std 802.11ad-2012 (Amendment to IEEE Std 802.11-2012, as amended by IEEE Std 802.11ae-2012 and IEEE Std 802.11aa-2012)*, pages 1–628, 2012.
- [7] Intel RealSense LiDAR L515 Camera. <https://www.intelrealsense.com/lidar-camera-l515/>, 2020.
- [8] Xilinx Zynq UltraScale+ RFSoC ZCU208 Evaluation Kit. <https://www.xilinx.com/products/boards-and-kits/zcu208.html/>, 2020.
- [9] IEEE Standard for Information Technology—Telecommunications and Information Exchange between Systems Local and Metropolitan Area Networks—Specific Requirements Part 11: Wireless LAN Medium Access Control (MAC) and Physical Layer (PHY) Specifications Amendment 1: Enhancements for High-Efficiency WLAN. *IEEE Std 802.11ax-2021 (Amendment to IEEE Std 802.11-2020)*, pages 1–767, 2021.
- [10] IEEE Standard for Information Technology—Telecommunications and Information Exchange between Systems Local and Metropolitan Area Networks—Specific Requirements Part 11: Wireless LAN Medium Access Control (MAC) and Physical Layer (PHY) Specifications Amendment 2: Enhanced Throughput for Operation in License-exempt Bands above 45 GHz. *IEEE Std 802.11ay-2021 (Amendment to IEEE Std 802.11-2020 as amendment by IEEE Std 802.11ax-2021)*, pages 1–768, 2021.
- [11] O. Abari, D. Bharadia, A. Duffield, and D. Katabi. Enabling High-Quality Untethered Virtual Reality. In *Proc. of the 14th USENIX NSDI*, page 531–544, 2017.
- [12] F. Adib, Z. Kabelac, and D. Katabi. Multi-person Localization via RF Body Reflections. In *Proc. of 12th USENIX NSDI*, pages 279–292, 2015.
- [13] F. Adib and D. Katabi. See Through Walls with WiFi! In *Proc. of the ACM SIGCOMM*, pages 75–86, 2013.
- [14] D. Bharadia, E. McMilin, and S. Katti. Full Duplex Radios. In *Proc. of the 27th ACM SIGCOMM*, pages 375–386, 2013.
- [15] Z. Chen, T. Zheng, C. Cai, and J. Luo. MoVi-Fi: Motion-robust Vital Signs Waveform Recovery via Deep Interpreted RF Sensing. In *Proc. of the 27th ACM MobiCom*, pages 392–405, 2021.
- [16] Z. Chen, T. Zheng, C. Hu, H. Cao, Y. Yang, H. Jiang, and J. Luo. ISACoT: Integrating Sensing with Data Traffic for Ubiquitous IoT Devices. *IEEE Communications Magazine*, pages 1–7, 2023.
- [17] C. Fiandrino, H. Assasa, P. Casari, and J. Widmer. Scaling Millimeter-Wave Networks to Dense Deployments and Dynamic Environments. *Proc. of the IEEE*, 2019.
- [18] Gao, Xiangyu and Xing, Guanbin and Roy, Sumit and Liu, Hui. Experiments with mmWave Automotive Radar Test-bed. In *Proc. of the 53rd IEEE Asilomar*, pages 1–6, 2019.
- [19] X. Gu, D. Liu, and B. Sadhu. Packaging and Antenna Integration for Silicon-based Millimeter-wave Phased Arrays: 5G and Beyond. *IEEE Journal of Microwaves*, pages 123–134, 2021.
- [20] J. Guan, A. Pajidimarri, A. Valdes-Garcia, and B. Sadhu. 3-D Imaging using Millimeter-wave 5G Signal Reflections. *IEEE Transactions on Microwave Theory and Techniques*, pages 2936–2948, 2021.
- [21] IETF. Precision Time Protocol Version 2 (PTPv2), 2017. Accessed: 2023-03-12.
- [22] M. A. Islam, G. C. Alexandropoulos, and B. Smida. Integrated Sensing and Communication with Millimeter Wave Full Duplex Hybrid Beamforming. In *Proc. of the 31st IEEE ICC*, pages 4673–4678, 2022.
- [23] W. Jiang, C. Miao, F. Ma, S. Yao, Y. Wang, Y. Yuan, H. Xue, C. Song, X. Ma, D. Koutsonikolas, et al. Towards Environment Independent device Free Human Activity Recognition. In *Proc. of the 24th ACM MobiCom*, pages 289–304, 2018.
- [24] K. Joshi, D. Bharadia, M. Kotaru, and S. Katti. Wideo: Fine-grained Device-free Motion Tracing using RF Backscatter. In *Proc. of the 12th USENIX NSDI*, pages 189–204, 2015.
- [25] D. Kunin, J. Bloom, A. Goeva, and C. Seed. Loss Landscapes of Regularized Linear Autoencoders. In *Proc. of the 36th ICML*, pages 3560–3569, 2019.
- [26] J. O. Lacruz, D. Garcia, P. J. Mateo, J. Palacios, and J. Widmer. mmFLEX: An Open Platform for Millimeter-Wave Mobile Full-Bandwidth Experimentation. In *Proc. of the 18th ACM MobiSys*, pages 1–13, 2020.
- [27] J. O. Lacruz, R. R. Ortiz, and J. Widmer. A Real-Time Experimentation Platform for Sub-6 GHz and Millimeter-Wave MIMO Systems. In *Proc. of the 19th ACM MobiSys*, page 427–439, 2021.
- [28] M. Li, Y. Meng, J. Liu, H. Zhu, X. Liang, Y. Liu, and N. Ruan. When CSI Meets Public WiFi: Inferring Your Mobile Phone Password via WiFi Signals. In *Proc. of the 23rd ACM CCS*, pages 1068–1079, 2016.
- [29] F. Liu, Y. Cui, C. Masouros, J. Xu, T. X. Han, Y. C. Eldar, and S. Buzzi. Integrated Sensing and Communications: Toward Dual-Functional Wireless Networks for 6G and Beyond. *IEEE Journal on Selected Areas in Communications*, pages 1728–1767, 2022.
- [30] F. Liu, L. Zhou, C. Masouros, A. Li, W. Luo, and A. Petropulu. Toward Dual-functional Radar-communication Systems: Optimal Waveform Design. *IEEE Transactions on Signal Processing*, pages 4264–4279, 2018.
- [31] C. X. Lu, S. Rosa, P. Zhao, B. Wang, C. Chen, J. A. Stankovic, N. Trigoni, and A. Markham. See through Smoke: Robust Indoor Mapping with Low-Cost MmWave Radar. In *Proc. of the 18th ACM MobiSys*, page 14–27, 2020.
- [32] S. Madani, J. Guan, W. Ahmed, S. Gupta, and H. Hassanieh. Radatron: Accurate Detection Using Multi-resolution Cascaded MIMO Radar. In *Proc. of the 17th ECCV*, pages 160–178. Springer, 2022.
- [33] S. Madani, S. Jog, J. O. Lacruz, J. Widmer, and H. Hassanieh. Practical Null Steering in Millimeter Wave Networks. In *Proc. of the 18th USENIX NSDI*, pages 903–921, 2021.
- [34] M. Mirza and S. Osindero. Conditional Generative Adversarial Nets. *arXiv preprint arXiv:1411.1784*, 2014.
- [35] K. I. Pedersen. Channel Parameter Estimation in Mobile Radio Environments using the SAGE Algorithm. *IEEE Journal on Selected Areas in Communications*, pages 434–450, 1999.

- [36] J. Pegoraro, J. O. Lacruz, M. Rossi, and J. Widmer. SPARCS: A Sparse Recovery Approach for Integrated Communication and Human Sensing in mmWave Systems. In *Proc. of the 21st ACM/IEEE IPSN*, pages 79–91, 2022.
- [37] Qualcomm. Qualcomm Wigig 60Ghz chipset QCA9500. <https://www.qualcomm.com/products/technology/wi-fi/qca9500>.
- [38] M. A. Richards. *Fundamentals of Radar Signal Processing*. McGraw-Hill Education, 2014.
- [39] I. P. Roberts, J. G. Andrews, H. B. Jain, and S. Vishwanath. Millimeter-Wave Full Duplex Radios: New Challenges and Techniques. *IEEE Wireless Communications*, pages 36–43, 2021.
- [40] S. K. Saha, Y. Ghasempour, M. K. Haider, T. Siddiqui, P. De Melo, N. Somanchi, L. Zakrajsek, A. Singh, O. Torres, D. Uvaydov, J. M. Jornet, E. Knightly, D. Koutsonikolas, D. Pados, and Z. Sun. X60: A Programmable Testbed for Wideband 60 GHz WLANs with Phased Arrays. In *Proc. of the 11th ACM WiNTech*, page 75–82, 2017.
- [41] M. A. Seifeldin, A. F. El-keyi, and M. A. Youssef. Kalman Filter-Based Tracking of a Device-Free Passive Entity in Wireless Environments. In *Proc. of the 6th ACM WiNTech*, page 43–50, 2011.
- [42] W.-L. Shen, K. C.-J. Lin, M.-S. Chen, and K. Tan. SIEVE: Scalable User Grouping for Large MU-MIMO Systems. In *Proc. of IEEE INFOCOM*, pages 1975–1983, 2015.
- [43] V. Singh, S. Mondal, A. Gadre, M. Srivastava, J. Paramesh, and S. Kumar. Millimeter-wave Full Duplex Radios. In *Proc. of the 26th ACM MobiCom*, pages 1–14, 2020.
- [44] M. Speth, S. A. Fechtel, G. Fock, and H. Meyr. Optimum Receiver Design for Wireless Broad-band Systems using OFDM. I. *IEEE Transactions on Communications*, pages 1668–1677, 1999.
- [45] S. Sur, I. Pefkianakis, X. Zhang, and K.-H. Kim. WiFi-assisted 60 GHz Wireless Networks. In *Proc. of the 23rd ACM MobiCom*, pages 28–41, 2017.
- [46] K. Wang, Z. Liu, Y. Lin, J. Lin, and S. Han. HAQ: Hardware-Aware Automated Quantization With Mixed Precision. In *Proc. of the 32nd IEEE/CVF CVPR*, 2019.
- [47] S. Wang, J. Huang, and X. Zhang. Demystifying Millimeter-Wave V2X: Towards Robust and Efficient Directional Connectivity under High Mobility. In *Proc. of the 26th ACM MobiCom*, 2020.
- [48] T. Wei and X. Zhang. Pose Information Assisted 60 GHz Networks: Towards Seamless Coverage and Mobility Support. In *Proc. of the 23rd ACM MobiCom*, page 42–55, 2017.
- [49] S. Wireless. TRX BF/01 User Manual. In *Sivers Semiconductors*, 2021.
- [50] C. Wu, F. Zhang, B. Wang, and K. J. Ray Liu. mmTrack: Passive Multi-Person Localization Using Commodity Millimeter Wave Radio. In *Proc. of the 39th IEEE INFOCOM*, pages 2400–2409, 2020.
- [51] Q. Yang, H. Wu, Q. Huang, J. Zhang, H. Chen, W. Li, X. Tao, and Q. Zhang. Side-Lobe Can Know More: Towards Simultaneous Communication and Sensing for MmWave. *Proc. of ACM UbiComp*, 2023.
- [52] F. Zhang, C. Wu, B. Wang, and K. J. R. Liu. mmEye: Super-Resolution Millimeter Wave Imaging. *IEEE Internet of Things Journal*, pages 6995–7008, 2021.
- [53] J. Zhang, X. Zhang, P. Kulkarni, and P. Ramanathan. OpenMili: A 60 GHz Software Radio Platform with a Reconfigurable Phased-Array Antenna. In *Proc. of the 22nd ACM MobiCom*, page 162–175, 2016.
- [54] J. A. Zhang, M. L. Rahman, K. Wu, X. Huang, Y. J. Guo, S. Chen, and J. Yuan. Enabling Joint Communication and Radar Sensing in Mobile Networks—A Survey. *IEEE Communications Surveys & Tutorials*, pages 306–345, 2021.
- [55] R. Zhao, T. Woodford, T. Wei, K. Qian, and X. Zhang. M-Cube: A Millimeter-Wave Massive MIMO Software Radio. In *Proc. of the 26th ACM MobiCom*, page 1–14, 2020.